SPECIAL ISSUE PAPER

Automatic segmentation of adherent biological cell boundaries and nuclei from brightfield microscopy images

**Rehan Ali · Mark Gooding · Tünde Szilágyi ·
Borivoj Vojnovic · Martin Christlieb · Michael Brady**

Abstract The detection and segmentation of adherent eukaryotic cells from brightfield microscopy images represent challenging tasks in the image analysis field. This paper presents a free and open-source image analysis package which fully automates the tasks of cell detection, cell boundary segmentation, and nucleus segmentation in brightfield images. The package also performs image registration between brightfield and fluorescence images. The algorithms were evaluated on a variety of biological cell lines and compared against manual and fluorescence-based ground truths. When tested on HT1080 and HeLa cells, the cell detection step was able to correctly identify over 80% of cells, whilst the cell boundary segmentation step was able to segment over 75% of the cell body pixels, and the nucleus segmentation step was able to correctly identify nuclei in over 75% of the cells. The algorithms for cell detection and nucleus segmentation are novel to the field, whilst the cell boundary segmentation algorithm is contrast-invariant, which makes it more robust on these low-contrast images. Together, this suite of algorithms permit brightfield microscopy image processing without the need for additional fluorescence images.

R. Ali (✉)
Department of Radiation Physics, Stanford University,
875 Blake Wilbur Drive, CC-G206, Stanford, CA 94305, USA
e-mail: rsali@stanford.edu

M. Gooding
Mirada Medical Ltd, Innovation House, Mill Street,
Oxford OX2 0JX, UK

T. Szilágyi · M. Brady
Department of Engineering Science, FRS FREng FMedSci Wolfson
Medical Vision Lab, University of Oxford, Parks Road,
Oxford OX1 3PJ, UK

B. Vojnovic · M. Christlieb
Gray Institute for Radiation Oncology and Biology, University of
Oxford, Old Road Campus Research Building, Oxford OX3 7QD, UK

Finally our *sephaCe* application, which is available at http://www.sephace.com, provides a novel method for integrating these methods with any motorised microscope, thus facilitating the adoption of these techniques in biological research labs.

1 Introduction

The past 5 years have seen resurgent interest in brightfield cell microscopy image analysis. Previously, the majority of algorithms for cell segmentation, registration, and tracking have been developed for fluorescence microscopy image data [23]; however, in some cases this is not the ideal approach. Fluorescence microscopy yields functional image data describing the localisation and magnitude of a specifically labelled biological object or process, but for some studies, anatomic image data of cellular structure provides better results. An example is quantifying cytosolic fluorescence for multiple cells, where the fluorescence signal may not be able to tell apart touching cells. Moreover, fluorescence microscopy cannot be used in certain applications such as studies of cellular radiation dose response, where the fluorescence energy can introduce unwanted sources of DNA damage through photobleaching [14]. In such cases, the cells have to be detected and segmented using non-fluorescence optics. Brightfield microscopy is the most ubiquitous and widely available form of microscopy, and therefore brightfield-specific solutions will have a wide audience. In addition, brightfield image analysis is perceived as a difficult problem which is interesting to solve in its own right, with the aim of developing more advanced image processing techniques.
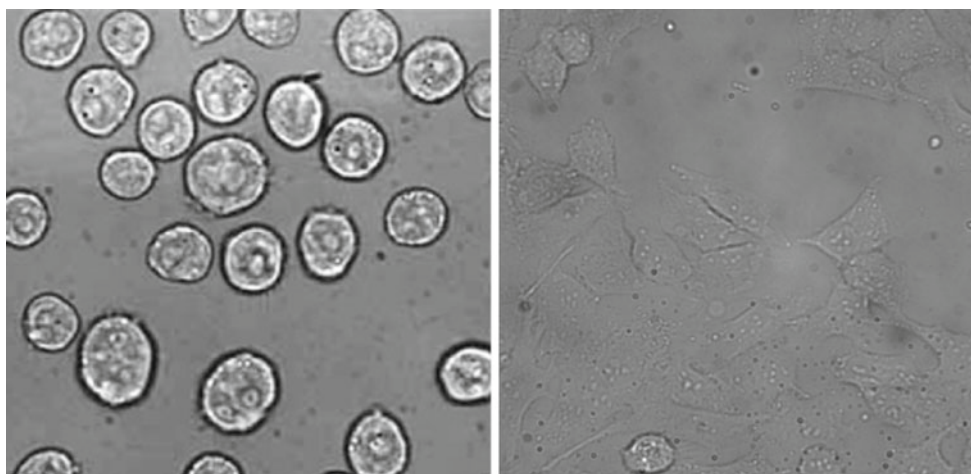
Fig. 1 Example of brightfield images of non-adherent (*left*) and adherent (*right*) HeLa cervical cancer cells. *Right* image is contrast-enhanced for clarity

A survey of the literature on brightfield cell boundary segmentation reveals a broad range of techniques, each of which show significant promise, but none which solve all of the key problems. Bradbury summarises the challenges involved, citing the broken boundary, poor contrast, partial halo, and overlapping cells as issues which confound the performances of her algorithms [7]. The prior work falls into three categories, based on physical models, statistical models, and active contours. In the first case, Paganin et al. developed a solution for the transport of intensity equation [27] which recovered phase information from amplitude-based images [21]. The technique produces attractive high-contrast images similar to those from phase contrast optics, which allow cells to be segmented through basic methods such as thresholding [10,30]; however, the results are often affected by low-frequency noise which can obscure the cells [22,31]. This is the result of inappropriate boundary conditions being provided for the equation. We have found that even after applying various techniques for reducing this noise, it would still be strong enough to cause segmentation methods based on thresholding or region-based analysis to fail [1]. In the case of statistical methods, Wu et al. [33] used a thresholded variance map followed by morphological operations; however, his technique was optimised for collagen-embedded cells which, when subtly defocused, presented a higher degree of contrast compared with cells in aqueous medium. Another approach used second moment statistics along with a Prewitt edge detector for identifying cells; however, it was very heuristic and required strong edge information [17]. Bradbury used spectral K-means clustering to separate variances in her images and presented interesting results; however, the accuracy is not quantified, her methods require manual initialisation, and they are unable to handle touching cells. A promising approach was proposed by Selinummi et al. [25]

whereby a z-stack was used to generate a 2D projection image which provided improved contrast. This technique was applied to cells with complex morphology, and its simplicity provides fast performance; however, the initial step of cell detection is performed either manually or on co-acquired nuclear fluorescence images. Finally, active snakes have been applied on rounded ovarian cells, first on brightfield images alone [28] and later using additional differential interference contrast images to improve the accuracy [29]. A limitation of snakes is that they have no inherent concept of interacting with neighbouring snakes, which could lead to results where touching cells are misidentified. Our method uses a similar active contour approach; however, it is adapted to handle touching cells.

In this paper, we present a series of integrated algorithms for identifying cells, segmenting the boundaries of cell bodies and nuclei, and registering images, all using brightfield image data. These algorithms are specifically designed for adherent biological cells, an area which has received relatively little attention to date. Adherent cells are predominantly used in cancer biology research and are the result of cells forming cell-surface interactions with glass or plastic surfaces. These attachments mimic in vivo intercellular interactions whilst still being easy to manipulate and image. The cell-surface linkages cause the cells to spread out over the surface, resulting in a reduction in surface curvature compared with non-adherent cells, which reduces the diffraction of light propagating through them. Their transparent nature renders them near-invisible when they are in focus, and the low curvature makes them harder to see when defocusing (Fig. 1). Cells typically become more visible during defocusing due to constructive interference (Fig. 3). Brightfield image processing with mammalian cell monolayers would greatly facilitate the development of automated

high-throughput time-lapse applications as the fixed position of the cells allows for repeated imaging at multiple time points, thus allowing studies where changes in intracellular fluorescence or cellular morphology can be monitored at the single-cell level. Such cytometric techniques have already been successfully developed for adherent yeast cells, which are more clearly visible due to their pronounced surface curvature [16], and extending them to mammalian cells would provide a tool that could yield new insights into cancer biology and other active research areas.

An ideal brightfield image processing platform for adherent cells would satisfy several requirements. It would be able to automatically and accurately detect adherent cells, separate touching cells, segment the boundaries of the cell body and key organelles, all without the aid of additional images from other microscopic modalities, and register brightfield images with misaligned fluorescence images. It would also be easy to integrate with most microscopes. This paper describes our free, open-source software suite, entitled *sephaCe* (short for seeing-the-phase-of-cells), which is available at http://www.sephace.com, and which satisfies all of these requirements for adherent cells. It is based on two previous versions which have introduced novel concepts into the brightfield image analysis field. In 2007, we combined the benefits of multiple slices at different levels of defocus with an integrated active contour framework [2], along with sophisticated methods of feature detection using local phase [12]. This was enhanced in 2008, resulting in an algorithm with improved accuracy and performance, which was adapted to multiple cell segmentation [3]. This paper substantially extends our previous work by introducing fully automatic cell detection and nucleus segmentation and wrapping it in a software framework that can integrate with any brightfield microscope with a motorised z axis (for controlling the level of focus). This allows easy implementation of a high-throughput brightfield image analysis system in any laboratory.

2 Methods

2.1 Experimental methods

2.1.1 Cell culturing

HeLa cervical cancer cells, HT1080 fibrosarcoma cells, SQ20B squamous cell carcinoma cells, and EMT6 murine mammary carcinoma cells were grown on coverslips (for the Nikon Eclipse 90i) or in optical vessels (for an inverted microscope, the Nikon Eclipse TE2000E) for a minimum of 24 h to allow them to adhere and spread out on the vessel surface and maintained in DMEM medium enriched with non-essential amino acids, sodium pyruvate, penicillin and streptomycin, glutamine, and foetal calf serum.

Table 1 The defocus distances required for mammalian adherent cells at different magnification levels

| Magnification	δz (μm) for segmentation	Δz (μm) for initialisation
10×	1	10
40×	10	25
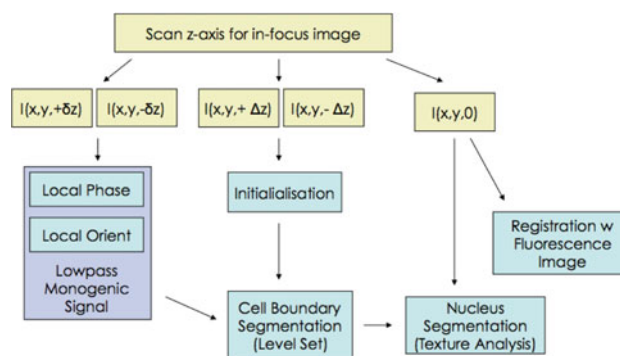
Fig. 2 Outline of the segmentation algorithm framework. Input images are denoted by *yellow boxes*

2.1.2 Microscopy

Transillumination brightfield images were captured using either a Nikon Eclipse 90i or an inverted Nikon Eclipse TE2000E epifluorescence microscope, controlled by software written by Vojnovic et al. at the Gray Institute [5], which allowed multiple fields-of-view (FOVs) to be predefined and imaged at preset z-axis depths. Samples were illuminated by a tungsten-halogen light bulb for brightfield image acquisition and imaged at 10× or 40× magnification with a 0.9 NA lens. Images were acquired at the distances given in Table 1 and were saved onto a networked file server as 8 bit image cytometry standard (ICS) format at a resolution of 1,024 × 1,344, describing a region of physical size 217 × 284 μm. Corresponding fluorescence images were acquired using Hoechst 33342 nuclear-specific dye (Sigma), using a DAPI-specific 430–490 nm band-pass filter, and using LysoTracker and MitoTracker dyes (Invitrogen Corporation™), using a TexRed 600–660 nm filter.

2.2 Image analysis

Figure 2 outlines the various brightfield image analysis algorithms and how they are integrated together. First the in-focus image is detected, either manually or automatically. This is a key reference position for our solution as the later steps require the acquisition of images which are symmetrically defocused either side of this point. The notation Δz (or δz for small distances) represents the defocusing distance, and $\Delta z = 0$ represents the in-focus image. Table 1 summarises
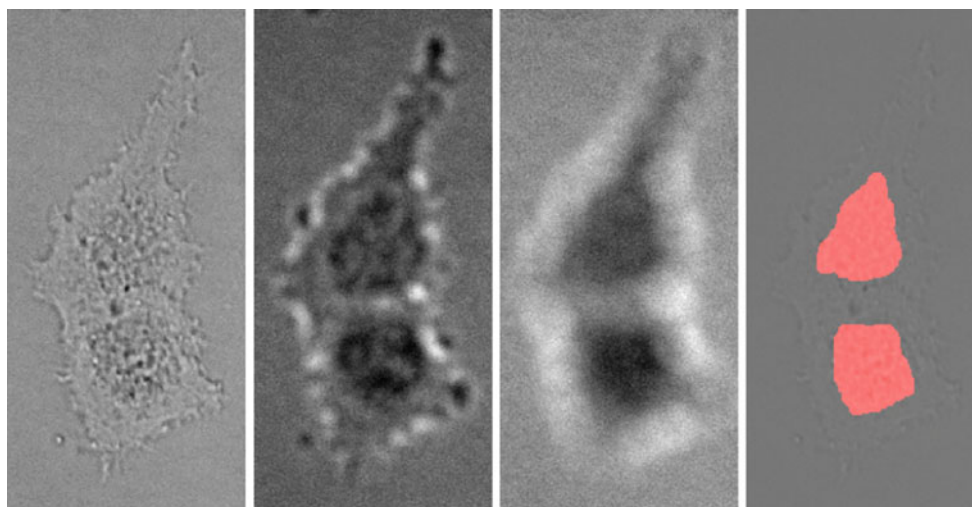
Fig. 3 Cell detection results (*left*-to-*right*) Brightfield images of an HT1080 cell, shown in-focus, at $-10\,\mu$m out of focus. and $-25\,\mu$m out of focus. The *third image* is used for cell detection. *Edges* between conjoined cells are indistinguishable when in-focus, but clearly resolvable when strongly out-of-focus (*right*) Initialisation result superimposed on in-focus image. Images are contrast-enhanced for clarity

the defocus distances required for each step. The second step is cell detection, which is used to initialise the cell boundary segmentation algorithm. This in turn is used to constrain the nucleus detection algorithm. Finally, registration with fluorescence data can be performed separately if required.

2.2.1 Locating the in-focus plane

An ideal in-focus brightfield image of unstained biological adherent cells has the property of appearing monotone, as the cells are virtually invisible and there are no out-of-focus components diffracting the light. This attribute can be used to locate the in-focus image. For a given image $I(x, y)$, of dimensions $[m \times n]$, the in-focus image is identified by using the entropy E of a given image,

$$E(I) = \int_{y=1}^{n} \int_{x=1}^{m} p(I(x, y)) \log p(I(x, y)) dx dy \qquad (1)$$

where $p(I(x, y))$ is the probability of the intensity value $I(x, y)$ derived from the image histogram. Entropy acts as a measure of focus which is minimised when $\Delta z = 0$ (i.e. when image information is minimal due to the invisible cells). This technique can be applied in both offline and online cases. In offline cases, the microscope writes a series of images at $1\,\mu$m intervals, and Eq. 1 is computed for each image. In the online case, the microscope software performs the optimisation, using the golden section search algorithm or a similar strategy. In both cases, the in-focus image will yield the global minimum value of E.

2.2.2 Cell detection

Individual cells are identified using a thresholding method based on strongly defocused images, where each cell is represented by a single blurred region which can be easily identified and segmented. This technique can be used to resolve touching cells, as shown in Fig. 3. Two strongly defocused images are used to generate a difference image,

$$\frac{\partial I}{\partial z} = I_1(+\Delta z) - I_2(-\Delta z) \qquad (2)$$

which is then thresholded using Otsu's automatic method [20], and labelled using connected components. A size filter is applied to remove small artefacts.

2.2.3 Cell boundary segmentation

The cell boundary segmentation algorithm relies on two components, outlined in Fig. 2. First, local phase and local orientation images are generated from a brightfield difference image using the monogenic signal framework, which is defined below. These are then used to guide the evolution of a level set-based active contour, which produces the final cell boundary segmentation.

Local phase is a commonly used concept for detecting features in signal processing. A suitably chosen even band-pass filter, $b_e(t)$, and its Hilbert Transform, $b_o(t)$, which is odd, can be applied to a signal $f(t)$ to yield information on its shape (local phase φ) and magnitude (local energy) at any given point. Local phase is defined in 1D as

$$\varphi(t) = \arctan\left(\frac{b_o(t) \otimes f(t)}{b_e(t) \otimes f(t)}\right) \qquad (3)$$

and describes the differential response of the signal to the odd and even quadrature filters. The result is a measure of the odd or even symmetry of the signal feature. This principle can be extended to multiple dimensions using the monogenic signal framework [12], where it is used as an image-based feature detector. In summary, the monogenic signal allows us to generate n-dimensional estimates of local energy, local phase and local orientation by generating odd nD filters from an even nD band-pass filter. This is done using the Riesz Transform through the use of two vector-valued filters h_1, h_2, which are defined in 2D as

$$h_1(u_1, u_2) = j \frac{u_1}{\sqrt{u_1^2 + u_2^2}} \qquad (4)$$

$$h_1(u_1, u_2) = j \frac{u_2}{\sqrt{u_1^2 + u_2^2}} \qquad (5)$$

where u_1, u_2 are the Fourier variables resulting from the Fourier transform of $I(x, y)$. This approach circumvents the traditional difficulty of finding odd 2D filters which are in quadrature to the even 2D filter. Local phase φ and local orientation θ are computed as described in [12], using the equations

$$\varphi = \arctan\left(\frac{h_2 \otimes I_e}{h_1 \otimes I_e}\right) \qquad (6)$$

$$\theta = \arctan\left(\frac{I_e}{\sqrt{(h_1 \otimes I_e)^2 + (h_2 \otimes I_e)^2}}\right) \qquad (7)$$

where I_e is the image convolved with the even 2D filter.

Typically, band-pass filters are used for the even filter, as the zero-DC component is important for providing the property of intensity invariance [6]. We discovered that if a low-pass filter is substituted in place of a band-pass filter, then a different type of result can be obtained which approximates the results of optical phase recovery algorithms (e.g. [21]). We recently outlined a possible mathematical connection, based on filter theory, between the two fields in a separate paper [4]. The advantages of our low-pass filter approach, compared with the phase recovery method of Paganin et al., are that it significantly reduces low-frequency noise associated with conventional phase recovery, and it also provides local orientation information which can be used to improve our algorithm. The low-pass filter is generated using a rotationally invariant filter [18],

$$f(r) = \frac{1}{r^{\alpha+\beta}} - \frac{1}{r^{\alpha-\beta}} \qquad (8)$$

where $\alpha = \beta = 0.25$.

A narrowband multi-region level set, based on the implementation by [15], is used to segment cell boundaries using the local phase and local orientation information. The level set framework is specifically required to compute the local orientation-based speed term, which is discussed below. The
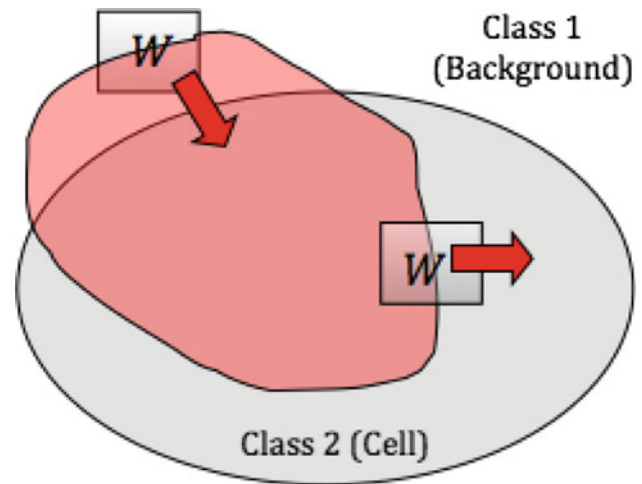
Fig. 4 Diagram of F_{phase} region term. A fixed size window W is applied to each point on the zero level set boundary (zero level set region shown in red). The local PDF is sampled in W and compared with the PDFs of the cell and the neighbouring class using Eq. 11. If the local PDF is more similar to the cell PDF then the F_{phase} term is positive (i.e. the level set expands at that point), whereas if it is more similar to the neighbouring PDF, the F_{phase} term is negative and the level set front retreats at that point

multi-region aspect is performed by maintaining a separate integer-valued class map alongside the level set. The cell detection result described earlier is used to initialise a signed distance function ϕ, which is then evolved using the level set PDE

$$\frac{d\phi}{dt} + F|\Delta\phi| \qquad (9)$$

where the speed term F regulating the level set evolution is given by

$$F = \alpha F_{\text{phase}} + \beta F_{\text{orientation}} + \gamma F_{\text{smooth}} + F_{\text{neighbour}} \qquad (10)$$

where α, β, γ are weighting coefficients for their respective speed terms.

The first term computes a probability distribution function (PDF)-based region term over the local phase image (Fig. 4). A local PDF is sampled using a moving window W at each point on the zero level set and is compared with the PDFs for the current cell class i and the neighbouring class j (which could be another cell or background). F_{phase} then compares these distributions using the term

$$F_{\text{phase}} = \frac{pdfv(W) \cdot pdfv(i)}{||pdfv(i)||} - \max_{j \neq i} \frac{pdfv(W) \cdot pdfv(j)}{||pdfv(j)||} \qquad (11)$$

where $pdfv(\cdot)$ is the vector form $[p_1 \ldots p_{255}]$ of the PDF, and p_i is the probability of intensity value i.

The second term uses local orientation information to drive the level set in the correct direction (Fig. 5). At each iteration, the direction of the normal gradient of the zero level
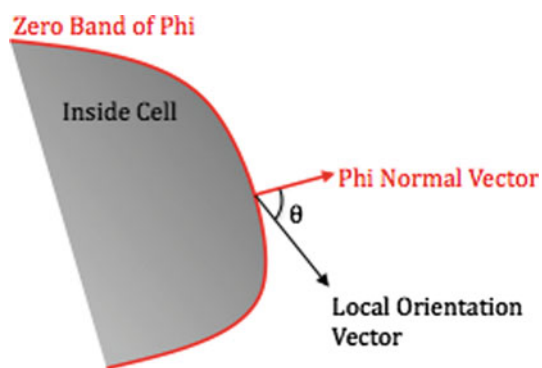
Fig. 5 Diagram of $F_{\text{orientation}}$ region term. At each point on the zero level set boundary, the angle of normal vector of the level set is compared with the local orientation value, using Eq. 12. If $cos(\theta) < 0$ then the level set retreats at that point, whereas if $cos(\theta) > 0$ then the level set expands

set, $\nabla(\phi = 0)$, is compared with the local orientation for that pixel. This provides a powerful driving term that guides the level set evolution along large distances (similar to the idea behind gradient vector flow [34]) towards the cell boundary feature and allows the boundary to escape from local minima. The term is defined by

$$F_{\text{orientation}} = cos(\theta_{\nabla\phi} - \theta_{LO}) \qquad (12)$$

where $\theta_{\nabla\phi}$ is the angle of the normal vector of the level set ϕ, and θ_{LO} is the local orientation angle. When the two are in agreement, ϕ experiences a positive expansion force, whilst if the two are opposing then ϕ will experience a negative contraction force.

The third term is a curvature-based regularising term, and the fourth term is a repulsion term which sets $F = -1$ if two cells are about to touch. This prevents region merging between two neighbouring cells. The weighting parameters are determined by receiver operating characteristic analysis and are set to $(\alpha, \beta, \gamma) = (5, 1, 1)$. The level set is solved to convergence.

2.2.4 Registration

Registration of brightfield images to images from the same or different modality (e.g. fluorescence) is performed in two stages. First, the in-focus brightfield image is used to compute a local energy map using the monogenic signal, using the equation

$$A = \sqrt{I_b^2 + (h_1 \otimes I_b)^2 + (h_2 \otimes I_b)^2} \qquad (13)$$

where I_b is the image convolved with the band-pass form of the rotationally invariant filter defined in Eq. 8, but where $\alpha = 3.25$ and $\beta = 0.25$. Second, rigid registration is performed. The registration algorithm uses normalised mutual information as a similarity measure, along with the $(1 + 1)$
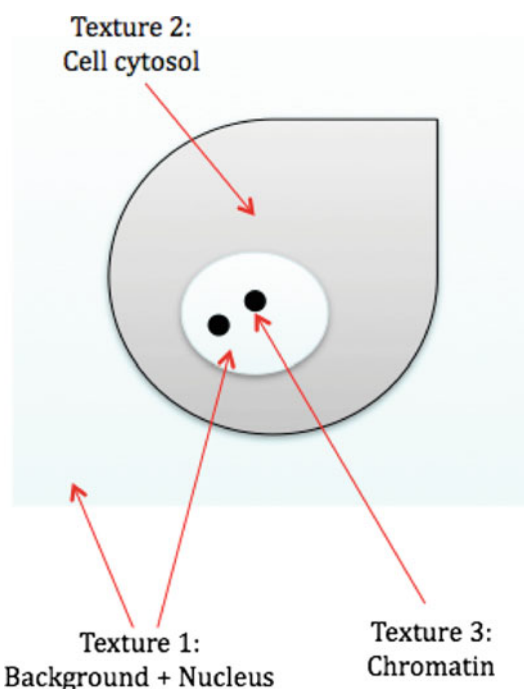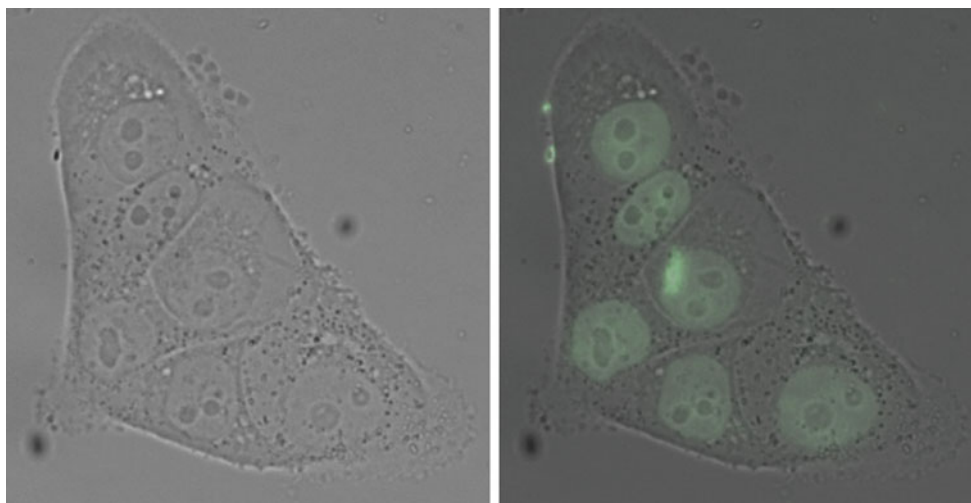

Fig. 6 Schematic of distribution of textures in brightfield image of adherent cells

evolutionary optimiser algorithm [26]. No initialisation is required. The algorithm assumes that the whole cell body is visible in both images.

2.2.5 Nucleus segmentation

Biological cells display a distinct difference in texture to the background; however, texture-based approaches to segmenting the cells are difficult to achieve due to the confounding level of background noise in the image data. As a result, texture-based segmentation on the in-focus image alone is difficult to perform robustly. Our boundary segmentation algorithm circumvents this issue by using a difference image, which relies on defocusing the microscope. However, small changes in focus can blur out fine texture, even using $\Delta z = \pm 1\,\mu m$ at $40\times$ magnification, thus ruling out this approach here. Fortunately, once the cell boundary has been segmented, it can be used to limit a texture analysis algorithm in order to resolve the cellular cytoplasm and nucleus of a specific cell. Figure 6 outlines the texture model for brightfield cells, where it can be seen that the nucleus is formed by an elliptical region with smooth texture equivalent to the non-cell background texture, which contrasts with the speckled texture of the cytosol. The Hoescht-stained fluorescence data in Fig. 7 confirms that this region is indeed the nucleus.

The quantitation of computational texture relies on the description of the local relationships between pixels. Felsberg et al. [13] defined intrinsic dimensionality as a fundamental

Fig. 7 Schematic of distribution of textures in brightfield image of adherent cells. Brightfield image of adherent SQ20B cells. Same image with Hoechst fluorescence stain overlaid in *green* to highlight the cell nucleus. Brightfield images are contrast-enhanced for clarity
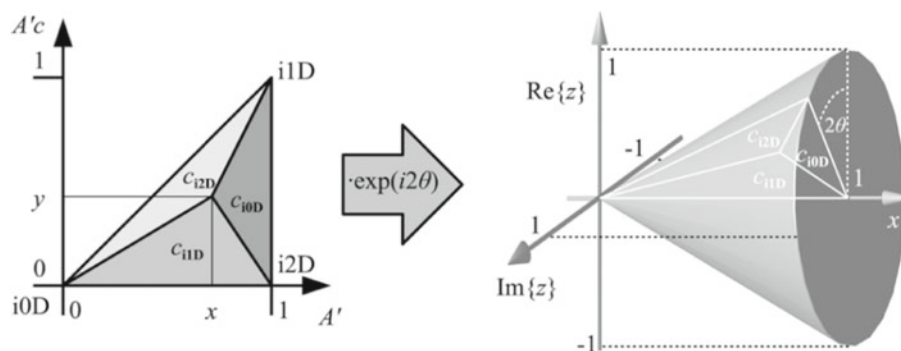
Fig. 8 Barycentric coordinates in a *triangle* (*left*) and a *cone* (*right*), used to compute the continuous intrinsic probabilities $ci0D, ci1D, ci2D$. In the triangle, the vertices represent the pure signal classes (i.e. when we have no doubt that a pixel is part of any of the above three classes, a rare case with real images) and anything between is represented by the rest of the points in the *triangle*. The *triangle* representation can be generalised to a *cone* for application to 2D data. Reprinted from Felsberg et al. (2008) with permission from Elsevier

signal property that relies on local connectivity. This allows the characterisation of each pixel based on its local neighbourhood into one of three classes, *i0d, i1d, i2d*, where *i0d* denotes a homogeneous patch (no change), *i1d* represents signals which have variance only along one orientation, i.e. lines and edges, and *i2d* denotes high curvature changes such as corners. Real signals are a mixture of these three classes; therefore, a valid separation between these is often hard. As a result, a continuous formulation of intrinsic dimensionality is used to allow the assignment of three probabilities, *ci0D, ci1D, ci2D*, which give a belief of how much the pixel is believed to belong to an *i0D, i1D, i2D* structure, respectively. In their seminal paper, the authors proposed a topological structure that captures the intrinsic signal classes in one model. In 2D this geometrical model takes the form of a triangle, which is presented in Fig. 8. The three barycentric coordinates for the point at location (x, y) are be defined as $(p_{ci0d}, p_{ci1d}, p_{ci2d}) = (1 - x, y, x - y)$. This triangle only explains the transition between the three signal classes

given one orientation for the ci1D class and is extended to all possibilities (in 2D) by the rotation along its i2D axes to form the cone shown in the figure. The estimation procedure for the probabilities is used as described in Felsberg's paper.

The estimated probabilities are used to segment the nucleus by fitting an ellipse to the *ci0D* probability map, limited within the bounds of the pre-determined cell boundary. A global search is performed using the ellipse parameters (x_0, y_0, a, b, θ). The optimal ellipse is the one yielding the maximum value for a fitness metric, which is determined as follows: The schematic in Fig. 6 outlines a model whereby the nucleus contains three features, namely a smooth texture, regions of dark chromatin, and a dark edge. Each of these features is insufficient (for example, the same smooth texture can be found in other parts of some cells, and the edge information is often sporadic). The fitness metric therefore combines both edge and region based information in order to locate the nucleus.

– An ellipse is generated using the current set of parameters from the search algorithm. An edge mask, m_e, and a region mask, m_r, are obtained from the ellipse.
– For the edge term, a local phase map is computed from the brightfield image using a band-pass filter (so that it acts as a feature detector), and thresholded at a value of 0.2 (thus delineating rut-shaped signal corresponding to the nucleus edges). This yields a binary image b_e which identifies edges.
– For the region term, the *ci0D* map is thresholded using Otsu's method to identify smooth textured regions and reject dark regions. This yields a binary image b_r.

These are used to compute the metric

$$f(x, y, a, b, \theta) = \frac{\lambda(m_e \cdot b_e)n_r}{n_e} + (m_r \cdot b_r) \qquad (14)$$

where n_r, n_e are the number of pixels representing the area and edge of the ellipse, which are used to normalise the two terms, and λ is a weighting factor that is set to 3.

2.2.6 Automated image processing

The *sephaCe* application was developed in Matlab/C++, and was set up on a Core 2 Duo 2.53Ghz PC with 3GB of RAM, with direct access to the networked directory containing the saved microscope images. Acquired ICS-format images are opened directly using LibIcs libraries from http://libics.sourceforge.net. *sephaCe* was set up to listen into the networked directory at 10-s intervals. On finding a new and complete set of images, *sephaCe* queues up the new job in an SQLite database and initiates its cell finding, boundary segmentation, and nucleus segmentation algorithms without any further manual intervention. A complete set of images is defined as each of the input brightfield images outlined in Fig. 2. The results are stored in the SQLite database for facilitated retrieval and querying.

3 Results

The initialization method was tested on cells from three different cell lines, HT1080 human fibrosarcoma cells, SQ20B human head and neck cells, and EMT6 murine mammary

**Table 2** Summary of automatic initialisation results for three different cell lines

Cell line	Cells	Correct	Split	Conjoined	FP
HT1080	285	240	16	18	5
SQ20B	41	0	0	41	0
EMT6	67	26	4	8	4

FP false positives

cells. Figure 3 shows a sample initialisation based on the strongly defocused images, demonstrating the ability of the technique to differentiate cells that appear to be touching when in-focus. The results are summarised in Table 2 and show that the technique was able to correctly identify 84% of HT1080s. A further 12% were incorrectly identified as being split into two or more regions or being a combination of two or more actual cells. The algorithm completely failed to detect 2% of cells.

The results for the other cell lines show that the results obtained with the HT1080s are a best case scenario. With the SQ20Bs, no cells were correctly identified, and all of the cells were identified as being conjoined with other cells. The SQ20B cells are known to be highly aggressive and can be seen to form tight interactions with each other. This results in a different defocusing behaviour, where the intracellular contrast does not improve with increasing defocus. The EMT6 cells were almost as challenging, and the method was only able to correctly identify 39% of them.

Figure 9 shows the results of the initialisation step, local phase, and local orientation estimation (using the low-pass Mellor-Brady filter), and the level set results for a set of HT1080 cells. The accuracy of our cell boundary segmentation algorithm was compared quantitatively against manual segmentations of individual cells performed by expert biologists, and qualitatively against fluorescence images (Fig. 10) acquired using MitoTracker and LysoTracker fluorophores that illuminate the cell body. The algorithm by Selinummi et al. was also evaluated using the same images ($\Delta z = 0$ and $\Delta z = \pm 10\,\mu m$ at $40\times$ magnification) [25]. Both algorithms are able to segment cell bodies accurately, even in cases where cells are touching. *sephaCe* was able to segment cells in cases where the brightfield image is corrupted by artefacts on the optics (Fig. 10, top). In some cell clusters, poor initializations can cause the algorithm to incorrectly segment cells (Fig. 10, bottom). The level of agreement between the automatically derived and manually drawn contours was quantified using three different measures, the Hausdorff distance [24], the DICE measure [11], and the percentage area that was correctly and falsely identified (True Positive and False Positive Pixels). Table 3 summarises these results. The *sephaCe* algorithm was able to segment 81% of HeLa cell body pixels (with a false-positive rate of 15% of the true cell area) and 75% of HT1080 cell body pixels (with a false positive rate of 5%). The latter cell type tends to exhibit larger ultra-thin regions which are difficult to segment. The high Hausdorff value relates the deviations from the true boundaries that are observed in the results. The Selinummi algorithm resulted in a slightly higher true positive rate and a significantly higher false positive rate. In addition, the Selinummi algorithm produced rough boundaries which overestimated the true boundary, whilst *sephaCe* produced smooth boundaries that underestimated the true
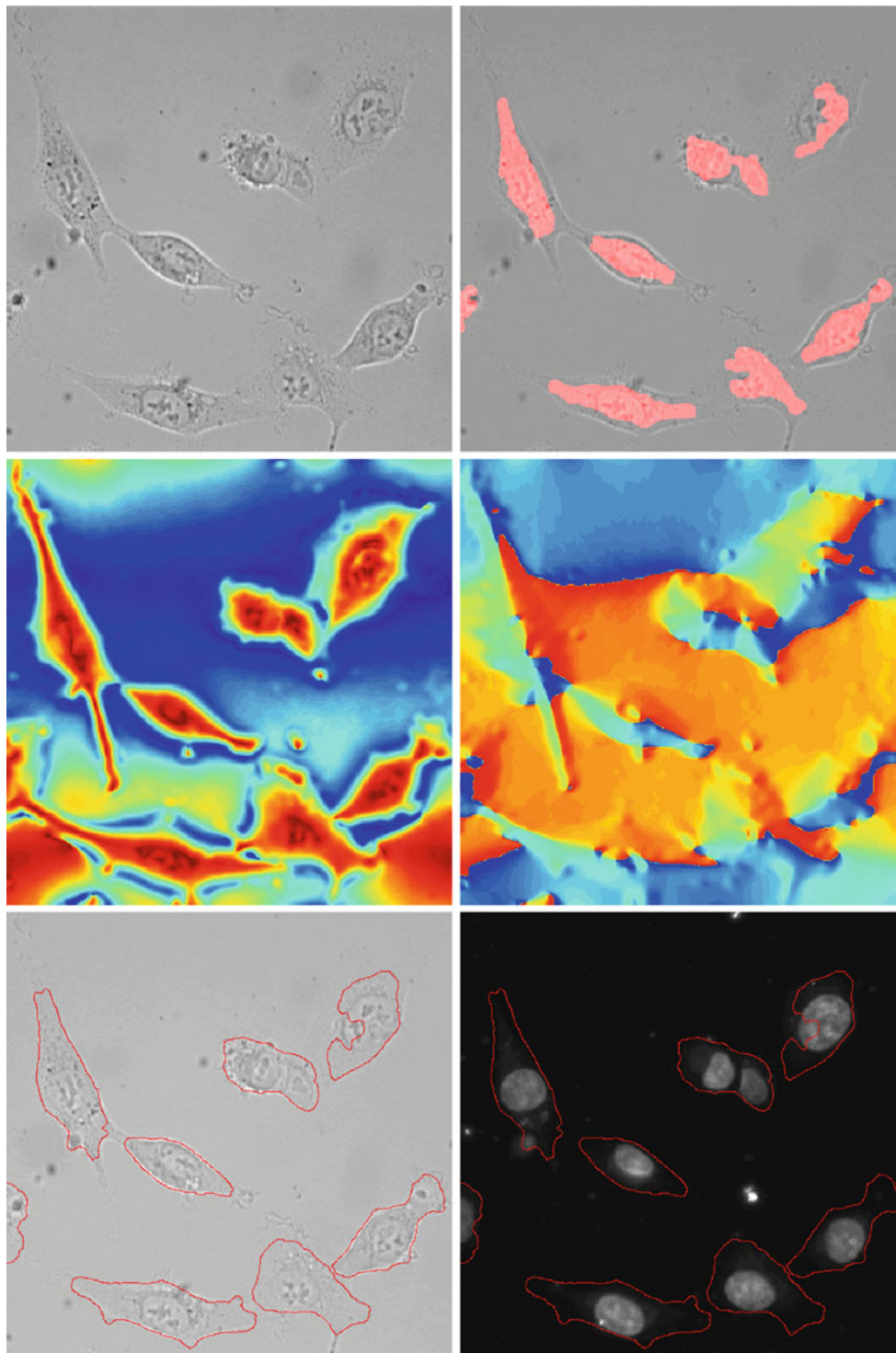
Fig. 9 (*top-left*) Adherent HT1080 cells imaged (40× magnification, $\Delta z = -2\,\mu m$). (*top-right*) Initialisation result overlaid in *red*. (*middle-left*) Local phase image, using low-pass filter. (*middle-right*) Local orientation image, using low-pass filter. (*bottom*) Final level-set segmentation boundary (*red contour*) overlaid on brightfield image (*left*) and Hoechst stained fluorescence image (*right*)

boundary. This underestimation mainly occurred in regions where the cell body became very thin, resulting in undetectable signals in the defocused images used to obtain the difference image. Intra-expert variability was assessed by obtaining manual segmentations from three experts and was found to be 4% of cell pixels.
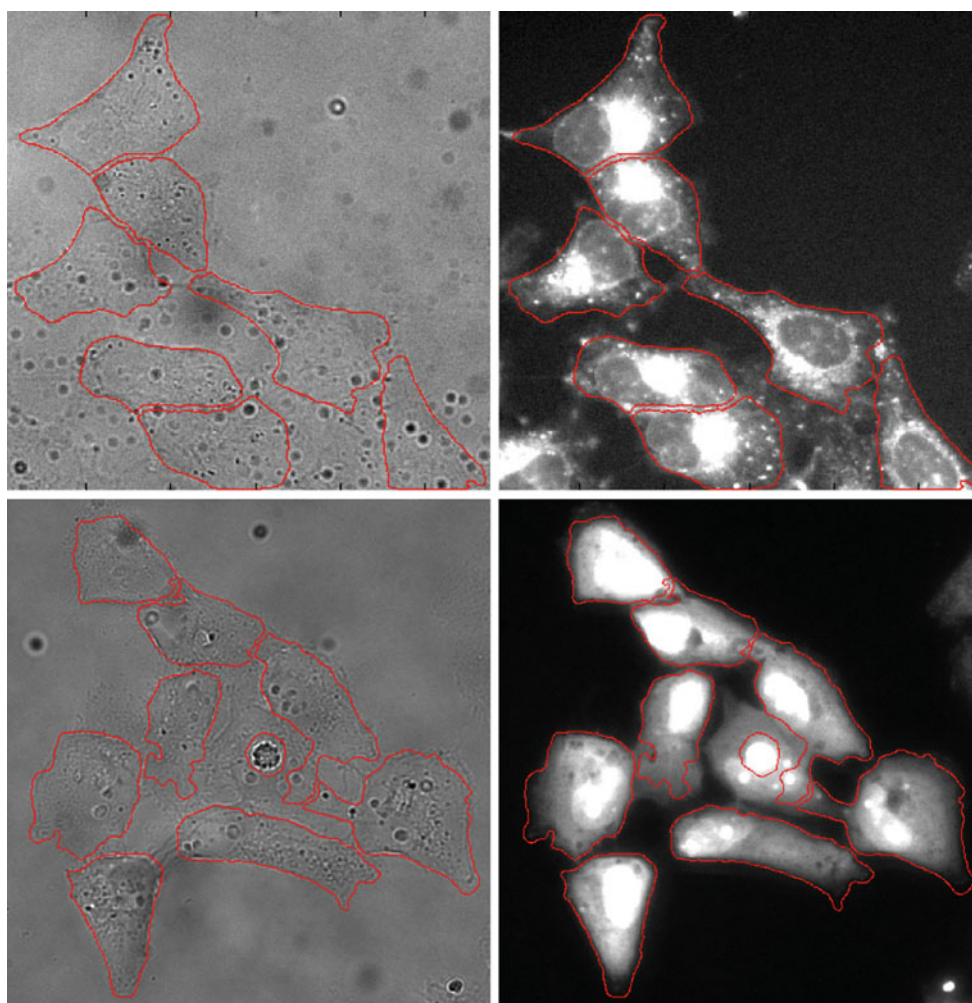
Fig. 10 Sample boundary segmentation results (*red contours*) super-imposed on brightfield and MitoTracker-stained fluorescence images of HeLa cells (*top row*) and HT1080 cells (*bottom row*). The *bottom row* shows a failed segmentation attempt for one of the central cells, which was caused by an inaccurate initialisation due to the dark artefact in the centre of that cell, which does not diffract light in the same way as the adherent cells. Brightfield images are contrast-enhanced for clarity

The nucleus segmentation algorithm was tested with different cell lines. Sample results can be observed in Fig. 11, and the results are summarized in Table 4. Segmentation results were classified according to three categories, Correctly Identified, Partially Identified, and Failure, which represented the algorithm correctly segmenting over 75%, between 50 and 75% and below 50% of the nucleus pixels, respectively. With HT1080 cells, the algorithm was able to correctly identify 70% of the nuclei, and it was able to partially identify an extra 20%. A significantly lower level of performance was found with EMT6 cells, where the algorithm correctly or partially identified 43% of the nuclei. With SQ20Bs, the algorithm failed to segment any nuclei.

The registration algorithm accuracy was assessed by obtaining brightfield and fluorescent images which were judged to be correctly aligned, and applying known displacements to the fluorescent image which were then corrected using the algorithm. The registration error is quantified by the metric

$$\epsilon = \sqrt{(t_x - \Delta x)^2 + (t_y - \Delta y)^2} \tag{15}$$

where (t_x, t_y) are the final translation coordinates in pixels, and $(\Delta x, \Delta y)$ is the initial displacement in pixels. Figure 12 shows a sample registration result. For displacements <110 pixels, the mean error was −2.3 pixels (standard deviation 2.2 pixels). A typical cell in the images used ($40\times$ magnification) has a length of approximately 200 pixels, suggesting that the algorithm is able to correct for displacements equivalent to half the length of the cells being imaged. At displacements greater than 110 pixels, the algorithm would fail to register the images.

The performance is outlined in Table 5. The algorithm was evaluated on images of size $1,344 \times 1,024$ pixels, representing a $40\times$ magnification brightfield image containing

Table 3 Summary of accuracy of cell boundary segmentation compared against manual segmentations of HT1080 and HeLa cells, comparing our *sephaCe* local phase level-set algorithm against the algorithm published in [25]

Measure	*sephaCe*	Selinummi
HT1080		
DICE	0.83 ± 0.09	0.72 ± 0.08
Hausdorff	55.4 ± 36.2	60.4 ± 28.6
TP pixels (%)	75.4 ± 15.1	79.4 ± 19.4
FP pixels (%)	5.4 ± 6.1	37.9 ± 26.0
HeLa		
DICE	0.82 ± 0.04	
Hausdorff	45.6 ± 10.9	
TP pixels (%)	81.3 ± 3.2	
FP pixels (%)	15.4 ± 4.73	

TP true positive, *FP* false positive. ($n = 106$ for HT1080; $n = 85$ for HeLa)
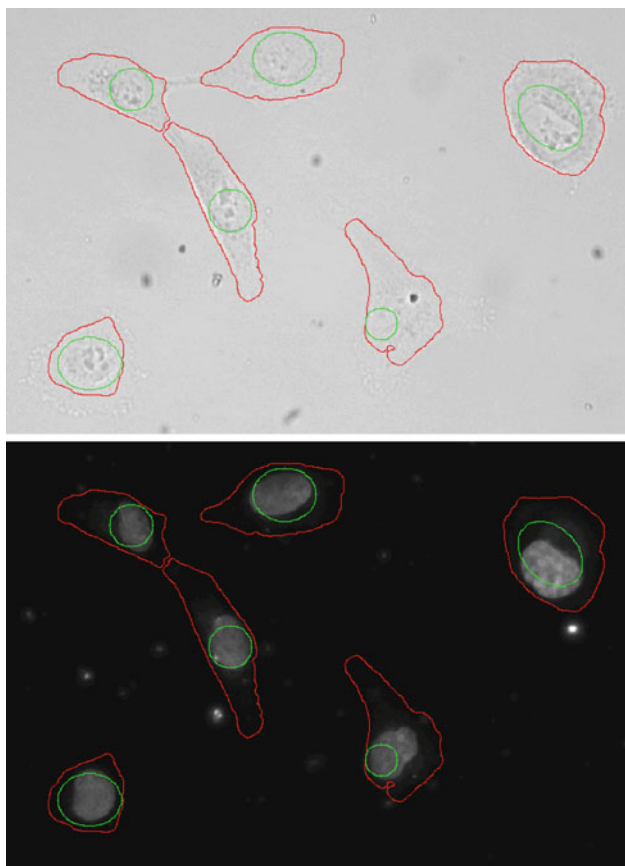
Fig. 11 Sample boundary and nucleus segmentation results, superimposed over brightfield image (*top*), and Hoescht-stained co-acquired fluorescence image (*bottom*). Segmented cell boundaries are in *red*, and nucleus segmentations are in *green*. Brightfield image is contrast-enhanced for clarity

an average of 10–15 cells. The initializing in-focus image detection and cell detection steps are the fastest, taking under

Table 4 Summary of automatic nucleus segmentation results

| Cell line	Cells	Correct	Partial	Failed
HT1080	132	94	30	12
SQ20B	41	0	0	41
EMT6	42	13	5	24

a second to perform. The level set evolution is significantly slower, taking approximately 20 iterations (120 s) to reach convergence. This is typical of the significant computational demands associated with computing active contours. The local orientation term is also a performance bottleneck, as it requires the computation of new angle values at the boundary at each iteration. The nucleus segmentation takes approximately 300 s due to the extensive parameter search required for the ellipse fitting. The fitness metric is very sensitive to the correct ellipse parameter set, and coarse-to-fine search algorithms failed to work. Finally, the registration takes an additional 60 s, but is invoked separately if the user believes that it is required.

4 Discussion

The problem of segmenting adherent cells from brightfield images is a challenging one due to the inherent lack of available contrast. Recently, several papers have described a number of steps towards solving this; however, certain problems remained unaddressed, namely the automation of cell detection without images from other modalities, the consistent delineation of cell boundaries in a contrast-independent manner, and the identification of subcellular organelles. In this paper, solutions have been proposed for each of these, resulting in a brightfield image analysis framework that can now be fully automated.

Our method comprises several steps, each of which is fully automatic. The cell detection step, which requires strongly defocused images, is able to correctly identify over 80% of cells from cell lines such as HT1080. These cells present similar surface curvature morphology when isolated and when touching other cells, and this allows them to be resolved during defocusing. The properties of HT1080s are similar to several other cancer cell lines, and we observed similar morphology and defocusing changes in HeLa, A549, HT29, and RKO cells, representing a range of tumor types. In contrast, aggressive cell lines such as the SQ20B form tight associations with their neighbours, and this interferes with a defocus-based method of cell separation. These cells are very difficult to tell apart, even for expert human observers. This step is fast to compute and can be used either to provide a reasonable cell boundary segmentation at $10\times$ magnification or to initialise the segmentation at higher magnifications. In both cases, providing a suitable cell line is used, it removes the requirement

Fig. 12 Sample brightfield to fluorescence registration results. Brightfield images are contrast-enhanced for clarity. Pre-registration brightfield (**a**) and LysoTracker-stained fluorescence **b** images are superimposed in (**c**), and show misalignment. **d** The superimposed images post-registration
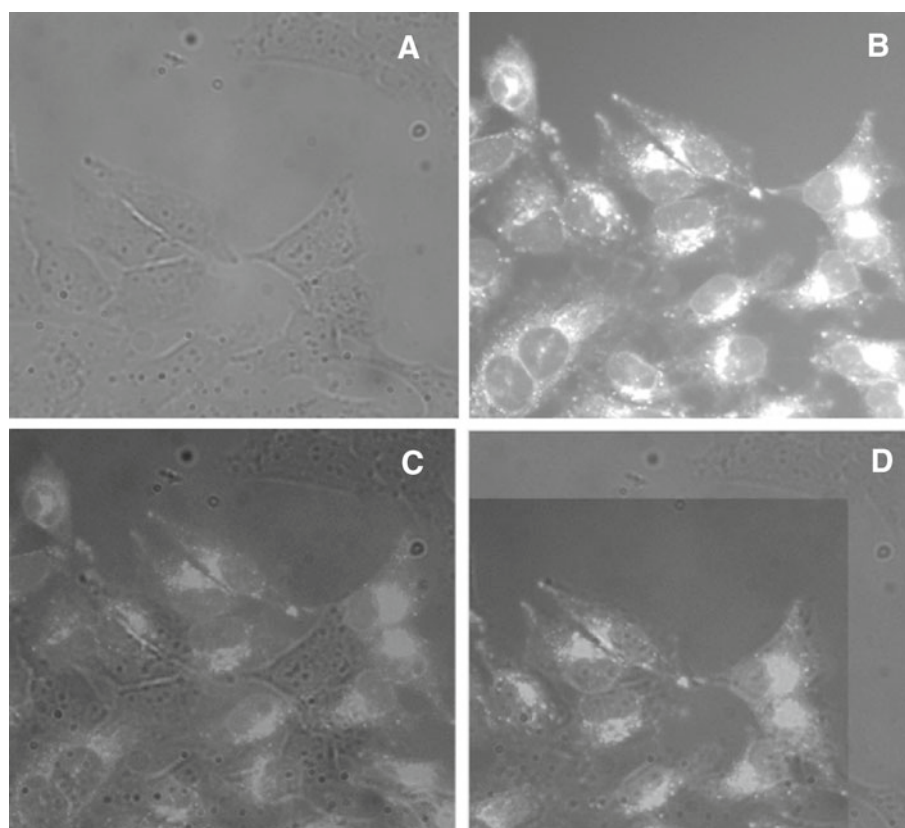
Table 5 Summary of algorithm performance for an image size $1{,}344 \times 1{,}024$ pixels, representing a $40\times$ brightfield image containing an average of 15 cells

Algorithm step	Approximate time (s)
In-focus image detection (offline)	≤ 1
Cell detection	≤ 1
Boundary segmentation	120
Nucleus segmentation	300
Registration	60

for ancilliary fluorescence images and thus has the potential to significantly facilitate experimental procedures.

The cell boundary segmentation step, which requires weakly defocused images, was able to segment over 75% of the cell body pixels for HT1080 and HeLa cells. It is robust against varying degrees of brightness and contrast, due to the use of local phase and local orientation, both of which are intensity-independent. The algorithm by Selinummi et al. was used to compare our results against. We found that both algorithms correctly segmented a similar number of cell body pixels. The Selinummi algorithm is fast to compute, but results in oversegmentation and rough edges. In addition, the results vary depending on the specific z-slices used. Various z-slices were tested, and the results presented in our

evaluation present a best-case scenario by using the same images ($\Delta z = \pm 10\,\mu\text{m}$ at $40\times$ magnification) as those used to test our algorithm. Finally, the projection metrics used by the Selinummi algorithm makes it sensitive to noise, as the noise contributions from each z-image are summed by the projection. In comparison, the use of difference images in our algorithm serves to cancel out most of the background noise, thus making it robust against several types of image noise found on microscope images, ranging from lens-based artefacts to uneven background illumination. The selection of the most appropriate algorithm will depend on the experimental context, and the Selinummi algorithm is provided in our *sephaCe* software as an alternative to the level-set based segmentation.

This paper also introduces the concept of organelle segmentation, which is new to the brightfield imaging field. On the HT1080 cell line, our novel texture and shape-based approach was able to identify most nuclei and correctly segment over 75% of them. The failed segmentations were primarily due to poor cell boundary segmentations, where the estimated boundary overlapped with the nucleus. In contrast, the method failed on SQ20B and EMT6 cells. This is likely to be due to our texture model in Fig. 6 being inappropriate for these cells, due to the cytosol containing regions of texture that are similar to that observed in the nucleus, thus confusing the algorithm. In addition, the algorithm is unable

to handle multiple nuclei in a cell, and therefore cannot handle SQ20B cells where the cell boundary step segments each cell cluster as individual cells.

A method for registering brightfield and fluorescence images is also proposed. Whilst also novel to the field, this is potentially of lesser utility, as it requires the fluorescent image to be acquired using a fluorophore which illuminates the whole cell body, whereas many fluorophores are highly specific to a particular region of the cell. In cases where the requirements are met, it is able to register cells which are misaligned by approximately 100 pixels.

Finally, the Matlab/C++ based *sephaCe* GUI allows these algorithms to be easily integrated with third-party microscopes, making all of the methods outlined in this paper available to cell biology researchers. The availability of graphical user interfaces for algorithms such as *sephaCe* and Cell Profiler [8], which can easily integrate with third party microscopes, promises to facilitate the implementation of true high-throughput imaging on any motorised brightfield microscope.

The field still contains areas for further research. These include the ability to segment cells from single images without the need for controlled defocusing. This would open up the technique to any non-motorised microscope, as well as to retrospective analysis of previously acquired image data. In addition, there is a high degree of variation in the structural properties of different cell lines, and techniques need to be developed that can cope with these. As an example, the SQ20B squamous head and neck cell line confounded our current set of algorithms, and represents a useful starting point for follow-up work. Finally, there is considerable scope to improve the performance of the algorithms presented here, which have been developed as proofs-of-concept and are thus unoptimised. Significant improvements can be yielded using faster numerical level set computation techniques (e.g. [19]), the use of GPU or CPU parallelisation (e.g. [9,32]), and improved search strategies, in order to develop these algorithms into near real-time high-throughput imaging techniques.

The ability to accurately segment adherent cells opens up a variety of promising application areas. We have already applied the technique to quantify fluorescence timelapse image data, where the resulting timeseries data were used to evaluate pharmacokinetic models of the uptake and efflux of ZnATSM, a hypoxia-selective fluorescent Positron Emisson Tomography tracer analogue [1]. In addition, it will be possible to perform single-cell level cytometry in a manner similar to [16], but with cell lines that are specifically of interest to cancer researchers. Such studies can replicate the results from flow cytometry, but with the added advantage of being able to perform high-resolution single-cell level analysis of the data in order to identify and quantify other potential parameters of interest.

References

1. Ali, R.: Applications of microscopy image analysis and modelling in characterising the mechanisms of hypoxia-mediated drug resistance. Ph.D thesis, University of Oxford, Oxford (2009)
2. Ali, R., Gooding, M., Christlieb, M., Brady, M.: Phase-based segmentation of cells from brightfield microscopy. In: Proceedings of the International Symposium Biomedical Imaging (ISBI), pp 57–60 (2007)
3. Ali, R., Gooding, M., Christlieb, M., Brady, M.: Advanced phase-based segmentation of multiple cells from brightfield microscopy images. In: Proceedings of the International Symposium Biomedical Imaging (ISBI), pp 181–184 (2008)
4. Ali, R., Szilagyi, T., Gooding, M., Christlieb, M., Brady, M.: On the use of lowpass filters for image processing with inverse laplacian models. J. Math. Imag. Vis. Under Rev. (2010)
5. Barber, P.R., Locke, R.J., Pierce, G.P., Rothkamm, K., Vojnovic, B.: Gamma-H2AX focicounting: image processing and control software for high-content screening. In: Proceedings of SPIE, San Jose, CA,USA, pp 64, 411M–64, 411M–10 (2007)
6. Boukerroui, M., Noble, D., Brady, A.: On the choice of band-pass quadraturefilters. J. Math. Imag. Vis. **21**, 53–80 (2004)
7. Bradbury, L.: Segmentation of bright-field cell images. Ph.D thesis, University of Waterloo, Ontario, Canada (2009)
8. Carpenter, A.E., Jones, T.R., Lamprecht, M.R., Clarke, C., Kang, I.H., Friman, O., Guertin, D.A., Chang, J.H., Lindquist, R.A., Moffat, J., Golland, P., Sabatini, D.M.: CellProfiler: image analysis software for identifying and quantifying cell phenotypes. Genome Biol. **7**(10), R100 (2006)
9. Cates, J., Lefohn, A., Whitaker, R.: GIST: an interactive, GPU-Based level set segmentation tool for 3D medical images. Med. Imag. Anal. **8**, 217–231 (2004)
10. Curl, C., Harris, T., Harris, P., Allman, B., Bellair, C., Stewart, A., Delbridge, L.: Quantitative phase microscopy: a new tool for measurement of cell culture growth and confluency in situ. Eur. J. Physiol. **448**, 462–468 (2004)
11. Dice, L.: Measures of the amount of ecologic association between species. Ecology **26**, 297–302 (1945)
12. Felsberg, M., Sommer, G.: The monogenic signal. IEEE Trans. Sig. Proc. **49**(12), 3136–3144 (2001)
13. Felsberg, M., Kalkan, S., Krüger, N.: Continuous dimensionality characterization of image structures. Imag. Vis. Comput. **27**(6), 628–636 (2009)
14. Folkard, M., Prise, K.M., Grime, G., Kirkby, K., Vojnovic, B.: The use of microbeamsto investigate radiation damage in living cells. Appl. Rad. Isot. **67**(3), 436–439 (2009)
15. Gooding, M., Kennedy, S., Noble, J.: Volume segmentation and reconstruction from freehand 3D ultrasound data with application to ovarian follicle measurement. Ultrasound Med. Biol. **34**(2), 183–195 (2008)
16. Gordon, A., Colman-Lerner, A., Chin, T., Benjamin, K., Yu, R., Brent, R.: Single-cell quantification of molecules and rates using open-source microscope-based cytometry. Nat. Methods **4**, 175–181 (2007)
17. Korzynska, A., Stronjy, W., Hoppe, A., Wertheim, D., Hoser, P.: Segmentation of microscope images of living cells. Pattern Anal. Appl. **10**(4), 301–319 (2007)

18. Mellor, M., Brady, M.: Phase mutual information as a similarity measure for registration. Med. Image Anal. **9**(4), 330–343 (2005)
19. Nilsson, B., Heyden, A.: A fast algorithm for level set-like active contours. Pattern Rec. Lett. **24**, 1331–1337 (2003)
20. Otsu, N.: A threshold selection method from gray-level histograms. IEEE Trans. Syst. Man Cybern. **9**, 62–66 (1979)
21. Paganin, D., Nugent, K.: Noninterferometric phase imaging with partially coherent light. Phys. Rev. Lett. **80**(12), 2586–2589 (1998)
22. Paganin, D., Barty, A., McMahon, P., Nugent, K.: Quantitative phase-amplitude microscopy. III. The effects of noise. J. Microsc. **214**, 51–61 (2004)
23. Rittscher, J., Machiraju, R., Wong, S.T.C.: Microscopic Image Analysis for Life Science Applications, 1st edn. Artech House Publishers, USA (2008)
24. Rote, G.: Computing the minimum Hausdorff distance between two point sets on a line under translation. Inf. Process. Lett. **38**, 123–127 (1991)
25. Selinummi, J., Ruusuvuori, P., Podolsky, I., Ozinsky, A., Gold, E., Yli-Harja, O., Aderem, A., Shmulevich, I.: Bright field microscopy as an alternative to whole cell fluorescence in automated analysis of macrophage images **4**(10):e7497 (2009). doi:10.1371/journal.pone.0007497
26. Styner, M., Brehbuhler, C., Szekely, G., Gerig, G.: Parametric estimate of intensity homogeneities applied to MRI. IEEE Trans. Med. Imag. **19**(3), 153–165 (2000)
27. Teague, M.: Deterministic phase retrieval: a green's function solution. J. Opt. Soc. Am. **73**, 1434–1441 (1983)
28. Tscherepanow, M., Zollner, F., Kummert, F.: Classification of segmented regions in brightfield microscope images. ICPR **06**(3), 972–975 (2006)
29. Tscherepanow, M., Nickels, N., Kummert, F.: Recognition of unstained live drosophila cells in microscope image. pp. 169–176. IMVIP, Los Alamitos (2007)
30. Veselov, O., Polak, W., Ugenskiene, R., Lebed, K., Lekki, J., Stachura, Z., Styczen, J.: Development of the IFJ single ion hit facility for cell irradiation. Radiat. Prot. Dosim. **122**, 316–319 (2006)
31. Volkov, V., Zhu, Y., Graef, M.D.: A new symmetrized solution for phase retrieval using the transport of intensity equation. Micron. **33**(5), 411–416 (2002)
32. Wang, K., Chang, A., Kale, L., Dantzig, A.: Parallelization of a level set method for simulating dendritic growth. J. Parallel Distrib. Comput. **11**, 1379–1386 (2006)
33. Wu, K., Gauthier, D., Levine, M.: Live cell image segmentation. IEEE Trans. Biomed. Eng. **42**(1), 1–12 (1995)
34. Xu, C., Prince, J.: Snakes, shapes and gradient vector flow. IEEE Trans. Image. Proc. **7**, 359–369 (1998)

Author Biographies

Mark Gooding completed his DPhil in Medical Imaging at the University of Oxford in 2004. His research interests include medical image segmentation and registration. After completing his DPhil, he worked as research assistant for Royal United Hospital, Bath, UK, and for the University of Oxford. He is currently a senior research scientist at Mirada Medical, Oxford, UK, but continues to work closely with academia on his research interests.

Tünde Szilágyi is a graduate student, reading for a DPhil at the Department of Engineering Science, University of Oxford. Her current research interests include understanding and detecting fibrosis in the context of cancer biology using mathematical models of molecular processes and image analysis.

Borivoj Vojnovic graduated from the University of Kent at Canterbury in 1972 in the department of Electronic Engineering. He obtained an MSc in Space Electronics, before joining the Biophysics and Engineering Section at the CRC Gray Laboratory, Mount Vernon Hospital. He obtained a PhD in Radiation Physics from the University of London in 1983 and developed instrumentation related to fast, ionising radiation-induced kinetic chemical processes, with application in areas of cancer biology. In 2007, he was appointed Professor of Biophysics Imaging at the University of Oxford, Medical Sciences School. His research interests include the application of advanced optical imaging, image processing and image analysis modalities for tissue and cellular imaging.

Rehan Ali is an SMIS Molecular Imaging Postdoctoral Fellow at Stanford University. His research interests are in using preclinical in vivo molecular imaging, image processing and mathematical modelling to predict tumor radiation resistance. He completed his DPhil in Biomedical Image Analysis at the University of Oxford in 2009.

Martin Christlieb works at the MRC/CRUK Gray Institute for Radiation Oncology and Biology at the University of Oxford. His main research interests are in molecular imaging. He has been with the Gray since 2006: previously he was attached to the Inorganic Chemistry Department at Oxford.

Michael Brady FRS FREng FMedSci is a member of the Department of Radiation Oncology and Biology at the University of Oxford, having recently retired as Professor of Information Engineering, in the Department of Engineering Science. He has received honorary doctorates from 6 universities, and was awarded the Whittle Medal by the Royal Academy of Engineering. Mike is also Founder of Mirada Medical Ltd, Matakina Ltd, and Guidance Ltd, and a Director of 4 other companies.